

## ARTICLE OPEN



# Single-crystalline nanoribbon network field effect transistors from arbitrary two-dimensional materials

Muhammad Awais Aslam<sup>1</sup>✉, Tuan Hoang Tran<sup>2</sup>, Antonio Supina<sup>3</sup>, Olivier Siri<sup>4</sup>, Vincent Meunier<sup>5</sup>, Kenji Watanabe<sup>6</sup>, Takashi Taniguchi<sup>7</sup>, Marko Kralj<sup>3</sup>, Christian Teichert<sup>1</sup>, Evgeniya Sheremet<sup>2</sup>, Raul D. Rodriguez<sup>2</sup> and Aleksandar Matković<sup>1</sup>✉

The last decade has seen a flurry of studies related to graphene nanoribbons owing to their potential applications in the quantum realm. However, little experimental work has been reported towards nanoribbons of other 2D materials. Here, we propose a universal approach to synthesize high-quality networks of nanoribbons from arbitrary 2D materials while maintaining high crystallinity, narrow size distribution, and straightforward device integrability. The wide applicability of this technique is demonstrated by fabricating molybdenum disulphide, tungsten disulphide, tungsten diselenide, and graphene nanoribbon field effect transistors that inherently do not suffer from interconnection resistance. By relying on self-aligning organic nanostructures as masks, we demonstrate the possibility of controlling the predominant crystallographic direction of the nanoribbon's edges. Electrical characterization shows record mobilities and very high ON currents despite extreme width scaling. Lastly, we explore decoration of nanoribbon edges with plasmonic particles paving the way for nanoribbon-based opto-electronic devices.

*npj 2D Materials and Applications* (2022)6:76; <https://doi.org/10.1038/s41699-022-00356-y>

## INTRODUCTION

The successful synthesis of graphene nanoribbons (NRs)<sup>1,2</sup> and their implementation in devices<sup>3,4</sup> has brought them at the forefront as building blocks for information processing in quantum and classical electronics<sup>5</sup>. Graphene NRs enable various functionalities including tunable band gap, high current carrying capability, long mean free path, localized spin and topological edge states<sup>5</sup>. Similarly, other two-dimensional (2D) material NRs can display edge specific properties such as ferromagnetism<sup>6,7</sup>, efficient catalysis<sup>8,9</sup>, and enhanced sensing abilities<sup>3,10</sup>. Moreover, a recent study about MoS<sub>2</sub> NRs demonstrated their potential for spintronics and quantum transport<sup>11</sup>. The development of 2D material NRs is largely driven by the needs in nanoelectronics, where three-dimensional (3D) gate-all-around architectures that employ nanotubes, nanorods, or NRs are considered as the likely solution to the arising scaling challenges<sup>12–14</sup>.

Despite all the possibilities that 2D material-based NRs hold, their sufficient quality, narrow widths, density, controlled edges, and high yield remain as technological challenges for realistic applications. The most widely used preparation methods are bottom-up chemical synthesis<sup>15–18</sup> and top-down lithography<sup>19–21</sup>. Chemical synthesis of NRs offers precise edge control and even allows synthesis of nanoporous graphene (NPG) ribbons with widths down to 1 nm. Such NPG systems are very appealing due to their ability to sieve as well as induce semiconducting behaviour in graphene<sup>22,23</sup>. However, bottom-up synthesis routes focus almost exclusively on graphene NRs, facing significant obstacles to develop more complex 2D materials or NR heterostructures. Moreover, the device channels suffer from electrical percolation issues and high junction (node) resistance<sup>3</sup>. Whereas, top-down lithography-based approaches do not offer a straight forward control over NR's alignment with respect to high

symmetry directions of the 2D material. They also cause interface contamination thereby degrading device performance and operation<sup>24</sup>.

Recently, Aljarb et al.<sup>25</sup> demonstrated a technique based on vicinal growth to fabricate NRs of arbitrary 2D materials e.g., (TMDCs). Although, the NRs produced by this approach are single crystals, the ribbon widths are rather large and non-uniform. The growth of these ribbons is also dependent on specific substrate, requiring an additional transfer step for their integration<sup>25</sup>. Vapour Liquid Solid (VLS) growth is another interesting method utilised for the NR synthesis<sup>11,26</sup>. Despite the fact that VLS uses silicon dioxide (SiO<sub>2</sub>) as a substrate, it employs salt and metal precursors that can be detrimental for device integration.

In this work we tackle the outlined challenges and demonstrate a universal method to fabricate NRs of arbitrary 2D materials, including graphene, hexagonal boron nitride (hBN), transition metal dichalcogenides TMDCs, and nanoribbon heterostructures with a width ranging from 6 to 100 nm. Our approach is based on epitaxially-grown organic needle-like nanostructures which self assemble along high-symmetry directions of 2D materials. We exploited these organic nano-needles as a mask through which 2D materials could be etched by oxygen plasma. This results in crystalline nanoribbon-networks (NRNs) with high edge-to-surface ratio and controlled predominant crystallographic edge-directions. To investigate the electrical performance of our NRNs and to show a challenging technological application, field effect transistors (FETs) were directly fabricated on Si/SiO<sub>2</sub> and Si/SiO<sub>2</sub>/hBN substrates. Besides their inherent single-crystalline nature, NRN-FETs were obtained without any additional transfer steps. TMDC NRN-based devices show outstanding electrical properties, including WS<sub>2</sub> and WSe<sub>2</sub> nanoribbons. We also observed ferroelectric switching for graphene NR devices due to water

<sup>1</sup>Institute of Physics, Montanuniversität Leoben, Franz Josef Strasse 18, 8700 Leoben, Austria. <sup>2</sup>Tomsk Polytechnic University, Lenina ave. 30, 634034 Tomsk, Russia. <sup>3</sup>Center for Advanced Laser Techniques, Institute of Physics, Bijenička cesta 46, 10000 Zagreb, Croatia. <sup>4</sup>Aix Marseille University CNRS CINaM UMR 7325, Campus de Luminy 13288, Marseille cedex 09, France. <sup>5</sup>Department of Physics, Applied Physics, and Astronomy, Rensselaer Polytechnic Institute, Troy, NY 12180, USA. <sup>6</sup>Research Center for Functional Materials, National Institute for Materials Science, 1-1 Namiki, Tsukuba 305-0044, Japan. <sup>7</sup>International Center for Materials Nanoarchitectonics, National Institute for Materials Science, 1-1 Namiki, Tsukuba 305-0044, Japan. ✉email: muhammad.aslam@unileoben.ac.at; aleksandar.matkovic@unileoben.ac.at

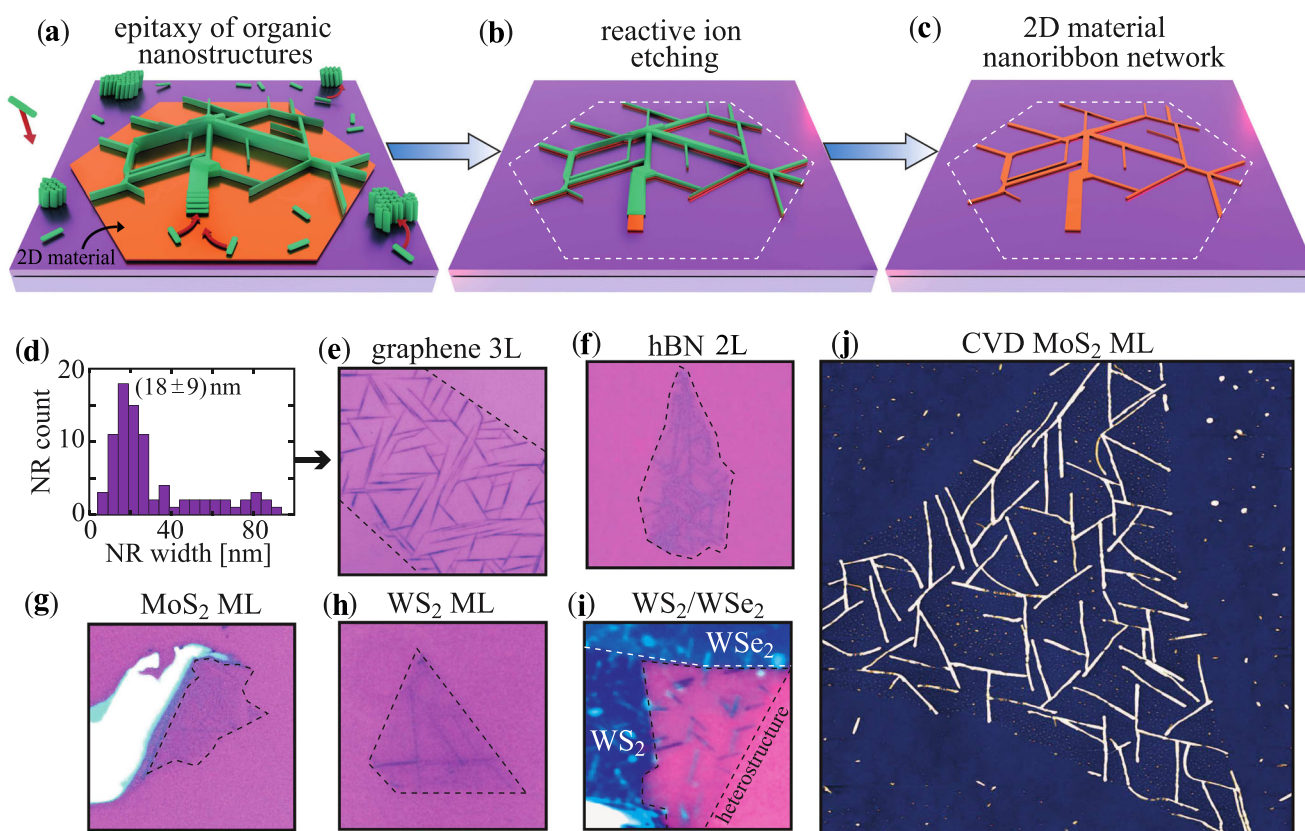


**Fig. 1 Fabrication of 2D material NRNs.** **a–c** Schematic representation of the key fabrication steps. **a** Organic nanostructures self-assembly and self-alignment. **b** After reactive ion etching. **c** NRN after removal of the sacrificial organic layer. **d** Histogram of NR widths for a graphene NRN shown in **e**. **e–i** Optical micrographs of various 2D material NRNs, presenting respectively NRNs of graphene, hBN, MoS<sub>2</sub>, WS<sub>2</sub>, and WS<sub>2</sub>/WSe<sub>2</sub> heterostructure. **j** AFM topography image of a NRN from chemical vapour deposition (CVD) Monolayer (ML) MoS<sub>2</sub> (22 × 22 μm<sup>2</sup>, z-scale 15 nm).

adsorption at the ribbon edges<sup>27</sup>. Our proposed method allows ribbons which do not suffer from high node resistance between interconnecting NRs, as the networks are ‘carved out’ from single crystals. To confirm this, we employ *in operando* Kelvin probe force microscopy (KPFM). To demonstrate our methods scalability and ultimate control over the NR edge-direction, we have fabricated predominant armchair and zigzag NRNs from a large-area MoS<sub>2</sub> ML obtained by chemical vapor deposited (CVD). Such high edge-density in nanoribbon network field effect transistors (NRN-FETs) has potential benefits in sensing applications and in tunable catalytic devices, especially when considering catalytic edge reactivity of MoS<sub>2</sub><sup>28,29</sup>. To go one step further, we illustrate edge-specific decoration of NRNs with silver nanoparticles, creating mixed-dimensional plasmonic heterostructures.

## RESULTS

### Fabrication of NRNs

Figure 1a–c depict the proposed NRN fabrication pathway. Detailed steps for MoS<sub>2</sub> and graphene are given in Supplementary Fig. 1. Typically, NRs of about 10–30 nm width distribution were realized as shown in Fig. 1d. By further optimization of the growth time, etching time, or selection of organic nano-structures based on shorter back bone (e.g., bi-phenylenes), the mean NRN width can be changed. The tunability of the mean width has been demonstrated by changing the growth time and is presented in Supplementary Fig. 2.

Organic molecules grow on 2D materials via van der Waals (vdW) epitaxy<sup>30</sup>. The molecules at the interface with the 2D material substrate adopt a flat-lying orientation and align their

$\pi$ -networks to optimize vdW interaction with the substrate<sup>31</sup>. Consequently, the molecules at the interface are ‘locked’ into preferential adsorption sites on the substrate and the growing crystallites adopt rotational commensuration with their 2D material support. This provides an inherent self-alignment with the substrates’ high symmetry directions, i.e., armchair or zigzag<sup>32–34</sup>.

After organic nanostructure growth, the hybrid organic/2D material stacks were precisely etched to form NRNs via exposure to oxygen plasma, i.e. reactive ion etching (RIE). An etch rate of ~1 layer in 3 s was established for graphene and TMDCs. Upon etching, the remaining organic molecules can either be left as an encapsulation layer<sup>35</sup> or removed by rinsing in chloroform or also by vacuum annealing. Our method allows for fabrication of monolithic NRNs of different exfoliated and CVD 2D materials, as demonstrated for graphene, hBN, MoS<sub>2</sub>, WS<sub>2</sub> and WSe<sub>2</sub> Fig. 1(e–j). Apart from individual 2D materials, in Fig. 1i we show NRN-heterostructures consisting of vertically stacked monolayer WS<sub>2</sub> (n-type) and bilayer WSe<sub>2</sub> (p-type), thus enabling atomically thin p-n junctions.

The structural integrity of NRs was probed by Raman and photoluminescence (PL) spectroscopies. Results for graphene NRs show extremely low values of (Intensity of the D peak/Intensity of the G peak) I<sub>D</sub>/I<sub>G</sub> peak ratios in the Raman spectra after etching of the flake into NRN (Supplementary Fig. 3 and Supplementary Table 1). Similarly, for ML MoS<sub>2</sub> (Supplementary Fig. 4) there are no defect activated peaks, which indicates high crystallinity of the fabricated nanoribbons. Figure 2a, b show results for the NR pairs (considering 3 layer MoS<sub>2</sub>) with ~70° relative inclination. They exhibited a prominent difference in the intensities of E<sub>2g</sub><sup>1</sup> and A<sub>1g</sub>

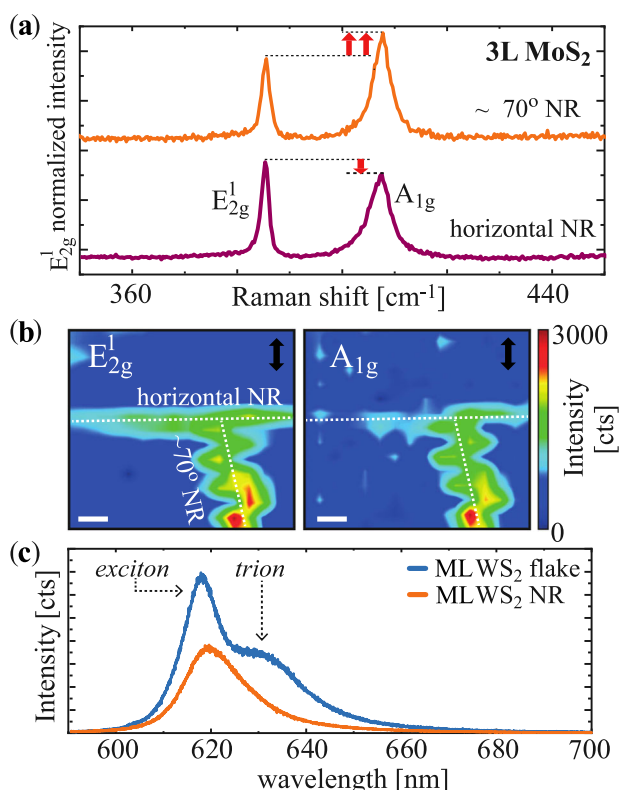


**Fig. 2 Evidence of structural integrity of the NRs.** **a** Raman spectra of the characteristic vibrational modes of MoS<sub>2</sub> showing the tri-layer flake before patterning, and two ribbons with  $\approx 70^\circ$  of relative inclination. The spectra are normalized with respect to the E<sub>2g</sub><sup>1</sup>-mode intensity, and relative changes of the A<sub>1g</sub> mode are indicated by horizontal dashed lines and red arrows. **b** Raman intensity maps of E<sub>2g</sub><sup>1</sup> and A<sub>1g</sub> modes of two intersecting NRs (scale-bar: 0.5  $\mu\text{m}$ ), highlighting a distinct variation of A<sub>1g</sub> mode as the ribbon direction is changed. The direction of linearly polarized light is indicated by black arrows. This is in agreement with the published result that the relative intensity of the A<sub>1g</sub> to E<sub>2g</sub><sup>1</sup> peaks is strongly dependent on the orientation angle of the material's crystallographic axes, for a fixed in-plane polarization<sup>60</sup>. **c** PL spectra of a ML WS<sub>2</sub> flake and corresponding NR, highlighting exciton and trion components.

Raman active modes. Such anisotropy for Raman modes of MoS<sub>2</sub> NRs<sup>36</sup> and MoS<sub>2</sub> flakes<sup>37</sup> was previously observed by changing the polarization configuration. The intensity of a Raman mode is proportional to the dot product of the Raman tensor with the light polarization. Since the NRs of both directions are etched out of the same flake, their crystallographic orientation, and consequently the dot products are the same. Thus, this anisotropy cannot be explained by the selection rules per se. Raman spectra for rotated nanoribbons and flake are shown in (Supplementary Fig. 5). Anisotropy has an apparent effect on the relative A<sub>1g</sub> mode intensity that warrants further investigation into its variations in narrow NRs. Furthermore, WS<sub>2</sub> NRs exhibited a dominant exciton peak and a suppressed trion peak in the PL measurements. This is due to a reduction in the free electron density over small widths (<30 nm) caused by the predominant oxygen terminated edges<sup>38,39</sup>. An example of the PL spectrum of WS<sub>2</sub> is presented in Fig. 2(c), comparing the initial ML flake and the resulting NR. The Raman spectra for the nanoribbon WS<sub>2</sub>/WSe<sub>2</sub> heterostructure is provided in the (Supplementary Fig. 6).

### Predominant crystallographic orientations of nanoribbons

To demonstrate that our proposed method offers control of NRs predominant crystallographic orientation, two different organic

molecules—parahexaphenyl (6P) and dihydrotetraazaheptacene (DHTA7)—were grown epitaxially on ML MoS<sub>2</sub> obtained by CVD. As their phenylene (6P) and acene (DHTA7) backbones could be seen as armchair and zig-zag motifs, respectively, and upon adsorption, molecular backbones will align with the corresponding high-symmetry directions of the 2D material substrate<sup>34,40,41</sup>. The control over the orientation of the predominant NR direction can be verified by using triangular CVD MoS<sub>2</sub> flakes that terminate with zig-zag edges due to the growth kinetics<sup>42–44</sup>. Figure 3a, b compares the NR directions and the triangular MoS<sub>2</sub> flake-edge directions, presenting 2D Fast Fourier Transform (2D-FFT) analysis of the atomic force microscopy (AFM) topography images (corresponding insets). In the case of 6P masks (Fig. 3a), predominant NR directions are tilted by  $(8.5 \pm 0.4)^\circ$  from the edge directions, i.e., NR edges are close to parallel with the zigzag crystallographic direction. By altering the backbone of the molecular mask (the case of DHTA7—Fig. 3b) the NR edges change predominantly following the armchair crystallographic direction. Moreover, employing other molecular species could allow controlling this angle for a particular 2D material of interest, and to exploit orientation specific properties for 2D materials<sup>45,46</sup> in the one-dimensional NR-regime.

### TMDC-NRN field effect transistors

Field-modulation of the NRNs was tested by fabricating two-terminal field-effect transistors (FETs) and investigating their transfer characteristics source-drain current vs source gate voltage  $I_D(V_{SG})$  at 77 K and 300 K. Van der Waals graphite electrodes were employed to probe electrical response of the devices between each step of the fabrication. Our proposed NRN fabrication method is compatible with conventional two-dimensional field effect transistor (2D-FET) fabrication schemes (as mask-lithography or e-beam lithography) since the 2D material films can be patterned into NRNs prior to the electrode fabrication. Figure 4a presents the scheme of the device geometry, and an optical micrograph for one of the WS<sub>2</sub>-NRN-FETs in the inset.

Figure 4b–d provide typical semi-logarithmic transfer curves at 300 K for flakes with organic nanostructures for WS<sub>2</sub>, MoS<sub>2</sub>, and WSe<sub>2</sub>, respectively and after patterning them into NRNs. For WSe<sub>2</sub> 10–15 nm hBN was used for bottom capping and NRN was patterned on top of it. MoS<sub>2</sub> and WS<sub>2</sub> devices exhibit an n-type behaviour whereas WSe<sub>2</sub> exhibited an ambipolar behaviour, both before and after patterning of the flakes into NRNs. A shift in the positive  $V_{SG}$  direction of the  $I_D(V_{SG})$  curves was observed after NRN formation, indicating p-type doping by the RIE process. On average,  $I_D(V_{SG})$  curves for MoS<sub>2</sub> devices showed a positive shift of 40 V after the NRN formation. This large positive shift can be attributed to electron depletion by the oxygen terminating NR-edges<sup>47</sup>.

The devices exhibited exceptional transfer characteristics even when SiO<sub>2</sub> was used as the gate dielectric. The performance of NRN-FETs could be further enhanced by employing high-K dielectric materials such as HfO<sub>2</sub><sup>48</sup>. An increase in the hysteresis was observed in the NR devices (except WSe<sub>2</sub>) which can be due to two possible mechanisms including high density of edges facilitating charge trapping/de-trapping mechanisms from adsorbates<sup>20</sup> or increased capacitive gating effect-traps due to SiO<sub>2</sub><sup>49</sup>. To investigate the origin of hysteresis the devices were annealed in vacuum at 400K which lead to reduction of hysteresis due to removal of adsorbates on the edges<sup>50</sup>. However, a full closure of the hysteresis was noted by performing low temperature measurements (77 K) as shown in (Supplementary Fig. 7) which points towards capacitive gating as the possible reason<sup>49</sup>.

Compared to the unetched flakes, the NRN-devices experienced a decrease of the  $I_D$ , as a consequence of the severely reduced channel widths when compared to the original 2D material-FET<sup>47</sup>. An increase in  $I_D$  and mobilities was observed when NRN-FETs are

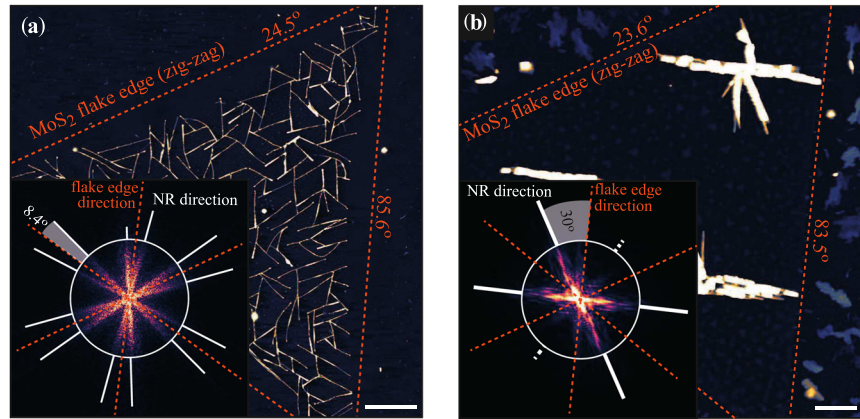


**Fig. 3 Orientation control of nanoribbons.** **a** (scale-bar: 5  $\mu\text{m}$ ) CVD MoS<sub>2</sub> NRN with ribbons nearly parallel to the flake edges (zigzag direction), using 6P molecules for the self-assembled mask. Inset shows 2D-FFT analysis of the NR directions with respect to the triangular flake edges. 2D Fast Fourier Transform (2D-FFT) image is rotated by 90° to represent real-space directions. **b** (scale-bar: 1  $\mu\text{m}$ ) Similar to **a** only using DHTA7 molecules for the self-assembled mask, and resulting in NRs in armchair direction (perpendicular to flake edges).

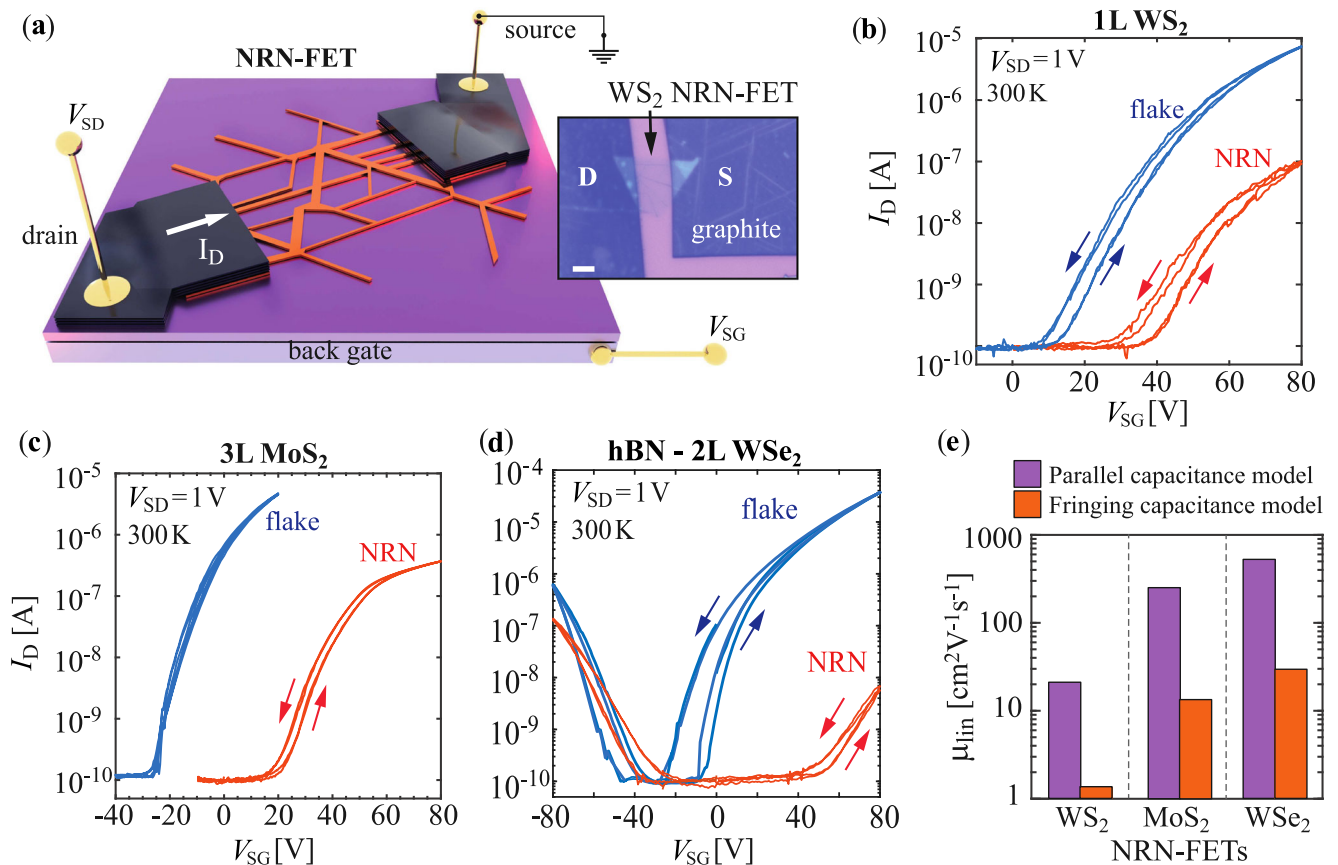


**Fig. 4 TMDC-NRN-FETs.** **a** Schematic diagram of a NRN-based FET utilizing vdW graphite electrodes. Inset of **a** shows an optical micrograph of a 3L WS<sub>2</sub> FET (scale-bar 5  $\mu\text{m}$ ). **b–d** Semi-logarithmic transfer curves of WS<sub>2</sub>, MoS<sub>2</sub>, and hBN-WS<sub>2</sub> FETs before and after patterning the flakes into NRNs. **e** Parallel and fringing capacitance apparent linear electron mobilities at 77 K, for the devices presented in **b–d**.

measured at low temperature (77 K). These observations confirm the presence of band transport in NRNs, as at low temperatures the contribution from phonons are minimized (Supplementary Fig. 8).

Figure 4e summarizes the apparent linear electron mobilities ( $\mu$ ) obtained from the  $I_D(V_{SG})$  curves measured at 77 K and calculated both by parallel and fringing capacitance models. Mobility plots are shown in Supplementary Fig. 8. The commonly used parallel capacitance model overestimates the mobilities when applied to

NRs as their widths are much smaller compared to the oxide thickness<sup>11</sup>. Therefore, taking into account the capacitance per unit area for the fringing capacitance model<sup>51</sup>, a more realistic area-specific gate capacitance can be expressed as:

$$C_{ox} \approx \epsilon_{ox} \epsilon_0 \left\{ \frac{\pi}{\ln \left[ 6 \left( \frac{t_{ox}}{W} + 1 \right) \right] W} + \frac{1}{t_{ox}} \right\} \quad (1)$$

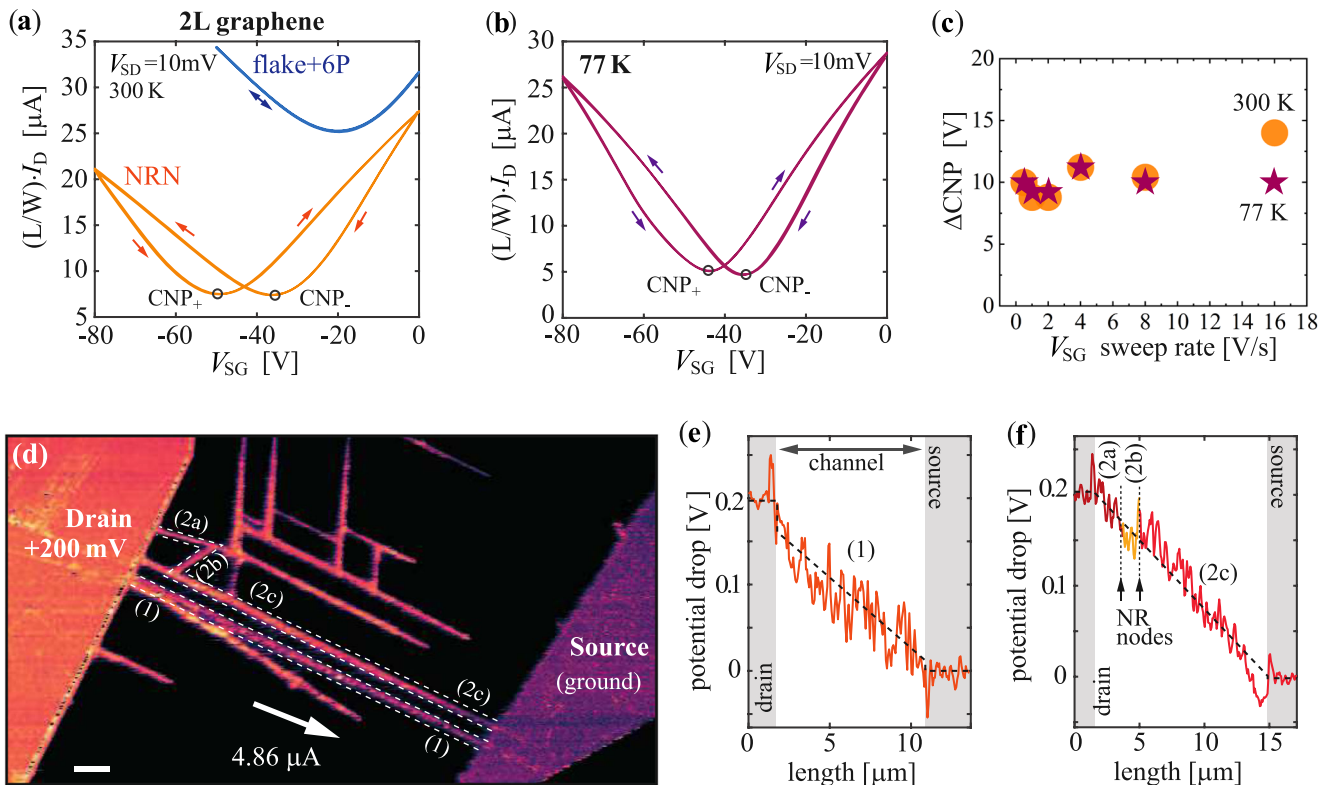


**Fig. 5 Graphene NRN-FETs.** **a** Length and width scaled transfer curves of the bi-layer graphene flake after organic nanostructure growth, and of the corresponding NRN-FET after annealing. Forward and reverse sweep direction is indicated by the arrows. **b** Length and width scaled transfer curves for graphene NRN-FET at 77 K, demonstrating that bi-modal switching persists at low temperature. **c** Difference in the forward and reverse bias charge neutrality point (CNP) positions as a function of the  $V_{SG}$  sweeping rate. **d** *in operando* FM-KPFM image of a graphene NRN-FET (scale-bar: 1  $\mu\text{m}$ ). Potential profile lines from the ribbons indicated by (1) and (2a–c) in sub-panel **d** are presented in **e** and **f**, respectively.

where  $t_{ox}$  is the oxide thickness and  $W$  is channel width. Effective channel length and width were estimated considering parallel and serial connections of NRs for each particular NRN-FET.

#### Graphene NRN-FETs and edge-induced ferroelectric effect

Besides very high mobilities  $\approx 1000\text{--}1200\text{ cm}^2\text{V}^{-1}\text{s}^{-1}$  (using the fringing capacitance model) graphene-based NRN devices exhibit pronounced hysteresis in the  $I_D(V_{SG})$ , see Fig. 5(a). The observed hysteresis  $\Delta\text{CNP}$  (difference between two CNPs) was not present in the original flakes, nor is introduced by the deposited organic nano-structures. The effect appears after the RIE in oxygen plasma once the samples are exposed to the ambient environment. This exposure allows the attachment of water molecules from the air to the oxygenated edges of the nanoribbons. The hysteresis remains in high-vacuum, at low temperatures Fig. 5b, and is practically independent of the  $V_{SG}$  sweep-rates Fig. 5c. Similar effect was predicted for edge-adsorbed water molecules and was observed for graphene-FETs with oxygen-plasma etched edges<sup>27</sup>. The orientation of water molecules can be changed due to the torque induced by the external electric field. The total field experienced by the graphene NRN is a sum of the gate-bias induced field and the net field produced by the edge-adsorbed water dipoles, yielding a robust bi-modal—ferroelectric—behavior of graphene NRN-FETs.

To rule out any causes of hysteresis due to trap-states the devices were measured in high vacuum ( $10^{-7}$  mbar), after vacuum annealing (at 410K for over 90 min), and were subjected to low temperature (77K) measurements. In all cases, the observed hysteresis was preserved. As the trapping is sensitive to temperature a significant quenching would occur at low

temperature<sup>52,53</sup>. This was observed for TMDC-based NRN-FETs, where the bi-stable states of the adsorbed water molecules at the ribbon edges are not expected. For graphene NRN-FETs at 77 K the hysteresis of the transfer curves is only slightly reduced as shown in Fig. 5b. In addition,  $V_{SG}$  sweep-rate dependent measurements were carried out both at 300 K and at 77 K. Figure 5c presents the  $V_{SG}$  sweep-rate dependence of the  $\Delta\text{CNP}$ , representing the negligible difference in the CNP position for the forward and the backward sweeps. This further helps us excluding any contributions from capacitive gating which acts on seconds time scale<sup>52</sup>. Lastly, to identify the temperature required for water dissociation from graphene NR edges the devices were annealed for various temperatures (373 K, 473 K and 573 K) under vacuum conditions. A large reduction of the hysteresis was observed after annealing the devices at 573 K (Supplementary Fig. 9) whereas no significant changes to the hysteresis were observed for lower temperature. A shift of the CNP towards negative  $V_{SG}$  was also noted. This is a direct indication of water removal which otherwise causes a p-type doping of graphene<sup>54</sup>. Our results point to the induced ferroelectric effect in oxygen-terminated graphene nanoribbon-FETs, which is very similar and more robust than observed previously for the oxygen-terminated flake-edges<sup>27</sup>. While ferroelectric-graphene nanoribbons and their integration into heterostructures are very interesting and promising pathways for future nanoelectronics, optoelectronics, neuromorphic electronics, and sensing applications, such research is beyond the scope of this study. To directly probe the resistivity of the nodes between the adjacent NRs and the potential drops across the NRN-FET channel *in operando* frequency modulated (FM) KPFM was performed on graphene NRN-FETs. Figure 5d presents a

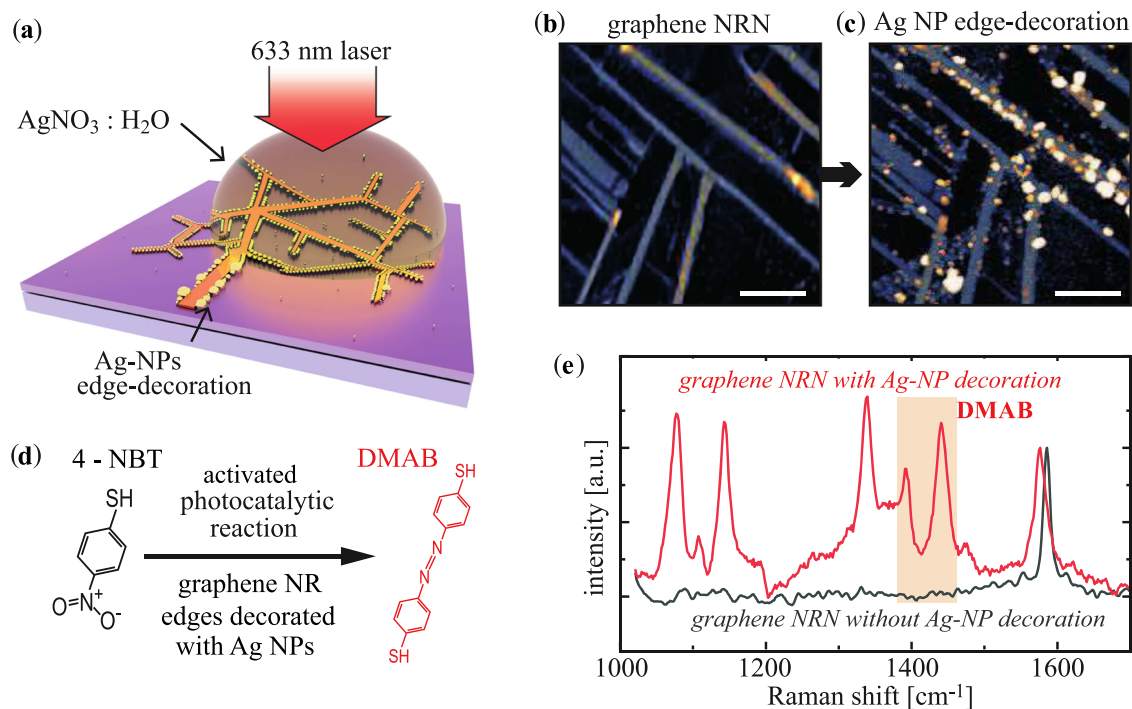


**Fig. 6** **Decoration of nanoribbon edges.** **a** Illustration of the process for the decoration of the NRNs with metallic nanoparticles, and **(b, c)** graphene NRN before and after edge-decoration with Ag NPs (scale bars 500 nm, z-scales 25 nm). **d** Dimerization of 4-NBT to DMAB and **(e)** demonstration of the photocatalytic activity and (surface-enhanced raman spectroscopy) SERS capability of the hybrid graphene-NRN + Ag-NP system.

contact potential difference (CPD) map across a graphene NRN-FET during operation.

To highlight the relevant potential drops across the channel, cross-sections marked in Fig. 5d are provided in Fig. 5(e, f). The transitions from the electrodes to the channel do not introduce any significant potential drops, as seen earlier for gold electrodes on both graphene and MoS<sub>2</sub><sup>55,56</sup>. Graphene NR labeled (1) interconnects between the source and drain electrodes, it exhibits an almost perfectly linear potential drop across the 10 μm long channel Fig. 5e. NRs labeled (2a–c) form a parallel connection to NR (1). No potential drop was observed at the nodes between (2a)–(2b) and (2b)–(2c), as indicated in Fig. 5f. Further, many more ribbons that do not bridge the source and drain electrodes, maintain a constant potential as these are not part of the current flow across the device. Above all, the consistent potential observed at all nodes is due to the translation of single-crystallinity of the original 2D material into the nanoribbon network. By not suffering from high node resistance, most of the potential drop of the provided  $V_{SD}$  bias is utilized for the transport along the NRs in the channel (Fig. 5d–f). As a consequence, our NRN FETs exhibit high on state currents and allow for high current modulation by the gate.

### Decoration of nanoribbons with plasmonic particles

To demonstrate high edge-to-surface ratio of our 2D material nanoribbon networks, we investigated edge-specific decoration of the NRs by metallic nanoparticles (NPs). Figure 6a schematically presents the decoration process. The details are provided in the methods section. The NR edges induce selective nucleation of Ag nanoparticles via the photo-activated reduction of Ag ions at the edges via electron transfer from graphene. Figure 6b, c present a graphene NRN before and after decoration with Ag NPs. Edge-specific decoration of 2D materials with metallic NPs was already demonstrated<sup>57</sup>, and utilizing NRN enhances the benefits of these hybrid systems.

To investigate the photocatalytic activity of the edge-decorated NPs, we use 4-nitrobenzenethiol (4-NBT) as a model for photocatalysis experiment. This is shown in Fig. 6d. The photocatalytic conversion of 4-NBT to p,p'-dimercaptoazobenzene (DMAB) has been intensively investigated<sup>58</sup>. Both Ag NP-decorated and bare graphene NRs were exposed to the solution of 4-NBT, and the resulting Raman spectra are shown in Fig. 5e. Without the NPs only the G-mode of the graphene NRs can be observed. However, edge decorated NPs not only enable surface-enhanced raman spectroscopy (SERS) signal, but also induce the desired photocatalytic reaction of 4-NBT into DMAB, as evident from the appearance of the DMAB characteristic Raman mode at ~1440 cm<sup>-1</sup> and ~1390 cm<sup>-1</sup>. These Raman modes are related to  $ag_{16}$  and  $ag_{17}$  vibrations of N=N of DMAB<sup>58</sup>. Such a photocatalytic reaction on nanoribbons decorated with plasmonic nanoparticles shows its future potential towards photocatalytic applications. In further studies, we will focus on employing 2D material-based NRN-FETs combined with edge-specific decorated plasmonic NPs, gaining an additional 'knob' via gate biasing. Such coupled mixed-dimensional plasmonic systems can be utilised in gate-controlled photocatalytic reactions, tunable SERS sensors, and high-sensitivity optoelectronic devices, however such experiments would go beyond the scope of this study.

### DISCUSSION

We propose a method to fabricate nanoribbon networks starting from arbitrary 2D materials, including WS<sub>2</sub> and WSe<sub>2</sub> NRs, and their heterostructures, which were not demonstrated until now. The method allows achieving NR widths below 20 nm while also enabling a straight-forward integration of the 2D material based NRNs into high-performance FETs with high yields of nanoribbon (Supplementary Table 2 and Supplementary Fig. 10). Further, with the appropriate choice of the self-aligned molecular masks control of the NR direction with respect to the crystallographic high-symmetry directions is achieved. Examined TMDC nanoribbon

network FETs exhibit band transport, maintain high carrier mobility values, clear off-states, high ON-state currents, and maintain stable operation over a large number of sweeping cycles (Supplementary Fig. 11).

By bridging between top-down and bottom-up approaches, our method provides high-quality NR connections (nodes) that do not act as scattering centers (high resistivity points), as proven by *in operando* KPFM of graphene-NRN FETs. Further, using graphene-NRN FETs we show bi-modal switching of the transfer curves which has been theoretically predicted, and thus far demonstrated only for graphene edges<sup>27</sup>. By Raman spectroscopy we have observed that MoS<sub>2</sub> ribbons with the different growth directions exhibit Raman anisotropy<sup>36</sup>. Our method facilitates both high crystallinity and large-area coverage without the high resistance issues of the adjacent nanoribbon nodes. In comparison, the bottom up approaches usually suffer from percolation and node resistance issues<sup>3</sup>, while the top-down approaches tend to introduce defects<sup>24</sup> in the ribbons yielding lower crystallinity.

Lastly, the high edge-to-surface ratios of our NRNs allowed us to selectively decorate the edges with plasmonic nanoparticles. These hybrid mixed-dimensional systems can provide a platform for next generation optoelectronic and plasmonic sensing devices due to the flexibility provided by our method for size tuning of the nanoribbons and the applicability of the process to heterostructures and vertical 2D material p-n junctions.

## METHODS

### 2D materials, organic masks, and device fabrication

Flakes of 2D materials were mechanically exfoliated from bulk crystal and transferred onto a 300 nm SiO<sub>2</sub>/Si substrate using commercially available Nitto tape and polydimethylsiloxane (Gel-Pak-DLG-X4). Monolayer and few layer flake thicknesses were identified via optical contrast, PL, and Raman measurements. Graphite flakes (10–50 nm thick kish graphite) were then transferred on 2D materials as electrodes to make device channels. 6P and DHTA7 nanostructures were grown on devices/flakes by hot wall epitaxy. The growth procedures were adopted from refs. <sup>34,41</sup>. MoS<sub>2</sub> triangular flakes were grown from solution-based CVD at atmospheric pressure similarly to the procedure in ref. <sup>59</sup>. The liquid Mo precursors used were NaMo and AHM in 1:1 ratio and dissolved in ultra-pure water at concentration of 200 ppm.

### Reactive ion etching

The reactive ion etching process was developed using an Oxford Plasma 80 plus RIE system. For all devices the forward power was kept at 80 W with an oxygen flow of 50 sccm under a pressure of 40 mTorr. Etching time was optimized according to the thickness of 2D materials.

### Electrical characterization

Electrical characterization of the flake- and NRN-FETs were done using Keithley 2636A Source-Meter attached to the Instec probe station. The samples were contacted with Au coated Ti electrical cantilever microprobes. Low temperature electrical measurements were performed using liquid nitrogen on a silver plate for thermal uniformity. The temperatures were monitored via mK2000 temperature controller connected to the probe station with a temperature resolution of 0.01 K.

### AFM and FM-KPFM Measurements

AFM and FM-KPFM measurements were performed using Horiba/AIST-NT Omegascope AFM system. Aselec probes were employed (spring constant ~ 42 N/m, resonant frequency ~ 70 kHz, tip radius below 30 nm). For width measurements 'Nanosensors' probes were

used (spring constant of 10–130 N/m, resonant frequency ~ 300 kHz and tip radius of 2 nm). For *in-operando* FM-KPFM experiments, the graphene-NRN-FETs were controlled by a Keithley 2636A sharing the same ground with the KPFM-setup. FM-KPFM measurements were carried out in a two-pass mode, with the probe lifted by 12 nm in the second pass. Topography and CPD images were processed in the open-source software Gwyddion v2.56. For topography images zero-order line filtering was applied and leveling of the base plane. For CPD images only zero order line filtering was applied.

### Micro-PL Measurements

All micro-PL and Raman measurements were performed using a Horiba LabRam HR Evolution confocal Raman spectrometer using 600 lines/mm and 1800 lines/mm gratings. A 532 nm laser source was used to excite the samples with an excitation power of 0.1–3.2 mW. The laser spot was focused by a 100×, 0.9 NA objective.

### NP edge-decoration and photocatalysis experiments

Ag deposition on graphene nanoribbons was carried out by photo-deposition method. 10 µl of 1 mM AgNO<sub>3</sub> was dropped on the sample. Thin glass was placed on top of the sample for ease of finding the region of interest. Red laser (633 nm) and objective 100x were used to irradiate the sample. Laser power, laser scanning speed and area were optimized to control the size of Ag NPs. For photocatalytic experiment, 0.1 mM 4-NBT with water to ethanol ratio 50:50 was prepared. Nanoribbon networks decorated with Ag NPs was immersed in this solutions overnight. After that, sample was washed and Raman spectra were recorded with NT-MDT Raman spectroscopy.

### DATA AVAILABILITY

Correspondence and the requests for the data and/or materials should be addressed to Aleksandar Matković.

Received: 11 June 2022; Accepted: 14 October 2022;  
Published online: 31 October 2022

## REFERENCES

- Li, X., Wang, X., Zhang, L., Lee, S. & Dai, H. Chemically derived, ultrasmooth graphene nanoribbon semiconductors. *Science* **319**, 1229–1232 (2008).
- Cai, J. et al. Graphene nanoribbon heterojunctions. *Nat. Nanotechnol.* **9**, 896–900 (2014).
- Chen, Z., Narita, A. & Müllen, K. Graphene nanoribbons: on-surface synthesis and integration into electronic devices. *Adv. Mater.* **32**, 2001893 (2020).
- Saraswat, V., Jacobberger, R. M. & Arnold, M. S. Material science challenges to graphene nanoribbons. *ACS Nano* **15**, 3674–3708 (2021).
- Wang, H. et al. Graphene nanoribbons for quantum electronics. *Nat. Rev. Phys.* **3**, 791–802 (2021).
- Pan, H. & Zhang, Y. W. Edge-dependent structural, electronic and magnetic properties of MoS<sub>2</sub> nanoribbons. *J. Mater. Chem.* **22**, 7280–7290 (2012).
- Slota, M. et al. Magnetic edge states and coherent manipulation of graphene nanoribbons. *Nature* **557**, 691–695 (2018).
- Lin, J. et al. Enhanced electrocatalysis for hydrogen evolution reactions from WS<sub>2</sub> nanoribbons. *Adv. Energy Mater.* **4**, 1301875 (2014).
- Karunadasa, H. I. et al. A molecular MoS<sub>2</sub> edge site mimic for catalytic hydrogen generation. *Science* **335**, 698–702 (2012).
- Lihter, M. et al. Electrochemical functionalization of selectively addressed MoS<sub>2</sub> nanoribbons for sensor device fabrication. *ACS Appl. Nano Mater.* **4**, 1076–1084 (2021).
- Li, X. et al. Nickel particle enabled width-controlled growth of bilayer molybdenum disulfide nanoribbons. *Sci. Adv.* **7**, eabk1892 (2021).
- Thomas, S. Gate-all-around transistors stack up. *Nat. Electron.* **3**, 728–728 (2020).
- Chen, M. L. et al. A FinFET with one atomic layer channel. *Nat. Commun.* **11**, 1–7 (2020).

14. Xu, L. Can carbon nanotube transistors Be scaled down to the sub-5 nm gate length? *ACS Appl. Mater. Interfaces* **13**, 31957–31967 (2021).
15. Jia, X., Campos-Delgado, J., Terrones, M., Meunier, V. & Dresselhaus, M. S. Graphene edges: a review of their fabrication and characterization. *Nanoscale* **2**, 86–95 (2011).
16. Barone, V., Hod, O. & Scuseria, G. E. Electronic structure and stability of semi-conducting graphene nanoribbons. *Nano Lett.* **6**, 2748–2754 (2006).
17. Jolly, A., Miao, D., Daigle, M. & Morin, J. F. Emerging bottom-up strategies for the synthesis of graphene nanoribbons and related structures. *Angew. Chem.* **132**, 4652–4661 (2020).
18. Bennett, P. B. et al. Bottom-up graphene nanoribbon field-effect transistors. *Appl. Phys. Lett.* **103**, 253114 (2013).
19. Han, M. Y., Özyilmaz, B., Zhang, Y. & Kim, P. Energy band-gap engineering of graphene nanoribbons. *Phys. Rev. Lett.* **98**, 206805 (2007).
20. Chen, S. et al. Monolayer MoS<sub>2</sub> nanoribbon transistors fabricated by scanning probe lithography. *Nano Lett.* **19**, 2092–2098 (2019).
21. Tapasztó, L., Dobrik, G., Lambin, P. & Biro, L. P. Tailoring the atomic structure of graphene nanoribbons by scanning tunnelling microscope lithography. *Nat. Nanotechnol.* **3**, 397–401 (2008).
22. Moreno, C. et al. On-surface synthesis of superlattice arrays of ultra-long graphene nanoribbons. *Chem. Commun.* **54**, 9402–9405 (2018).
23. Moreno, C. et al. Bottom-up synthesis of multifunctional nanoporous graphene. *Science* **360**, 199–203 (2018).
24. Zhou, Y. & Loh, K. P. Making patterns on graphene. *Adv. Mater.* **22**, 3615–3620 (2010).
25. Aljarb, A. Ledge-directed epitaxy of continuously self-aligned single-crystalline nanoribbons of transition metal dichalcogenides. *Nat. Mater.* **19**, 1300–1206 (2020).
26. SLi, S. Vapour-liquid-solid growth of monolayer MoS<sub>2</sub> nanoribbons. *Nat. Mater.* **17**, 535–542, (2018).
27. Caridad, J. M. et al. A graphene-edge ferroelectric molecular switch. *Nano Lett.* **18**, 4675–4683 (2018).
28. Salazar, N., Rangarajan, S., Rodríguez-Fernández, J., Mavrikakis, M. & Lauritsen, J. V. Site-dependent reactivity of MoS<sub>2</sub> nanoparticles in hydrodesulfurization of thiophene. *Nat. Commun.* **11**, 1–9 (2020).
29. Wang, H. et al. Structural and electronic optimization of MoS<sub>2</sub> edges for hydrogen evolution. *J. Am. Chem. Soc.* **141**, 18578–18584 (2019).
30. Koma, A. Van der Waals epitaxy for highly lattice-mismatched systems. *J. Cryst. Growth* **201**, 236–241 (1999).
31. Hlawacek, G., Khokhar, F. S., van Gastel, R., Poelsema, B. & Teichert, C. Smooth growth of organic semiconductor films on graphene for high-efficiency electronics. *Nano Lett.* **11**, 333–337 (2011).
32. Matković, A. et al. Epitaxy of highly ordered organic semiconductor crystallite networks supported by hexagonal boron nitride. *Sci. Rep.* **6**, 1–10 (2016).
33. Wang, J. Probing the crystallographic orientation of two-dimensional atomic crystals with supramolecular self-assembly. *Nat. Commun.* **8**, 1–8 (2017).
34. Vasić, B. et al. Molecules on rails friction anisotropy and preferential sliding directions of organic nanocrystallites on two-dimensional materials. *Nanoscale* **10**, 18835–18845 (2018).
35. Ha, T. J., Akinwande, D. & Dodabalapur, A. Hybrid graphene/organic semiconductor field-effect transistors. *Appl. Phys. Lett.* **101**, 033309 (2012).
36. Wu, J. B. et al. Monolayer molybdenum disulfide nanoribbons with high optical anisotropy. *Adv. Opt. Mater.* **4**, 756–762 (2016).
37. Ji, J. et al. Giant magneto-optical Raman effect in a layered transition metal compound. *PNAS* **113**, 2349–2353 (2016).
38. Cong, C., Shang, J., Wang, Y. & Yu, T. Optical properties of 2D semiconductor WS<sub>2</sub>. *Adv. Opt. Mater.* **6**, 1700767 (2018).
39. Kwon, Y., Kim, K., Kim, W., Ryu, S. & Cheong, H. Variation of photoluminescence spectral line shape of monolayer WS<sub>2</sub>. *Curr. Appl. Phys.* **18**, 941–945 (2012).
40. Kratzer, M., Matkovic, A. & Teichert, C. Adsorption and epitaxial growth of small organic semiconductors on hexagonal boron nitride. *J. Phys. D: Appl. Phys.* **52**, 383001 (2019).
41. Matković, A. et al. Light assisted charge propagation in networks of organic semiconductor crystallites on hexagonal boron nitride. *Adv. Funct. Mater.* **29**, 1903816 (2019).
42. Van Der Zande, A. M. et al. Grains and grain boundaries in highly crystalline monolayer molybdenum disulfide. *Nat. Mater.* **12**, 554–561 (2013).
43. Zhu, D. et al. Capture the growth kinetics of CVD growth of two-dimensional MoS<sub>2</sub>. *npj 2D Mater. Appl.* **1**, 1–8 (2017).
44. Zhou, W. et al. Intrinsic structural defects in monolayer molybdenum disulfide. *Nano Lett.* **13**, 2615–2622 (2013).
45. Li, F. et al. Strain improving the performance of a flexible monolayer MoS<sub>2</sub> photodetector. *Adv. Electron. Mater.* **12**, 1900803 (2019).
46. Arab, A. & Li, Q. Anisotropic thermoelectric behavior in armchair and zigzag mono- and fewlayer MoS<sub>2</sub> in thermoelectric generator application. *Sci. Rep.* **5**, 1–12 (2015).
47. Liu, H., Gu, J. & Peide, D. Y. MoS<sub>2</sub> nanoribbon transistors transition from depletion mode to enhancement mode by channel-width trimming. *IEEE Electron Device Lett.* **33**, 1273–1275 (2012).
48. Lee, G. H. et al. Flexible and transparent MoS<sub>2</sub> field-effect transistors on hexagonal boron nitride-graphene heterostructures. *ACS Nano* **7**, 7931–7936 (2013).
49. Park, Y., Baac, H. W., Heo, J. & Yoo, G. Thermally activated trap charges responsible for hysteresis in multilayer MoS<sub>2</sub> field-effect transistors. *App. Phys. Lett.* **108**, 083102 (2016).
50. Kaushik, N. et al. Reversible hysteresis inversion in MoS<sub>2</sub> field effect transistors. *npj 2D Mater. Appl.* **1**, 1–9 (2017).
51. Liao, A. D. et al. Thermally limited current carrying ability. *Phys. Rev. Lett.* **106**, 256801 (2011).
52. Wang, H., Wu, Y., Cong, C., Shang, J. & Yu, T. Hysteresis of electronic transport in graphene transistors. *ACS Nano* **4**, 7221–7228 (2010).
53. Singh, A. K. & Gupta, A. K. Reversible control of doping in graphene-on-SiO<sub>2</sub> by cooling under gate-voltage. *J. Appl. Phys.* **122**, 195305 (2017).
54. Melios, C., Giusca, C. E., Panchal, V. & Kazakova, O. Water on graphene review of recent progress. *2D Mater.* **5**, 022001 (2018).
55. Yu, Y. J. et al. Tuning the graphene work function by electric field effect. *Nano Lett.* **9**, 3430–3434 (2009).
56. Matković, A. et al. Interfacial band engineering of MoS<sub>2</sub>/Gold interfaces using pyrimidine-containing self-assembled monolayers toward contact-resistance-free bottom-contacts. *Adv. Electron. Mater.* **6**, 2000110 (2020).
57. Tanaka, N., Nishikiori, H., Kubota, S., Endo, M. & Fujii, T. Photochemical deposition of Ag nanoparticles on multiwalled carbon nanotubes. *Carbon* **47**, 2752–2754 (2009).
58. Dong, B., Fang, Y., Xia, L., Xu, H. & Sun, M. Is 4-nitrobenzenethiol converted to p, p'-dimercaptoazobenzene or 4-aminothiophenol by surface photochemistry reaction? *J. Raman Spectrosc.* **42**, 1205–1206. (2011).
59. Marion, I. D. et al. Atomic-scale defects and electronic properties of a transferred synthesized MoS<sub>2</sub> monolayer. *Nanotechnology* **29**, 305703 (2018).
60. Liang, L. & Meunier, V. First-principles Raman spectra of MoS<sub>2</sub>, WS<sub>2</sub> and their heterostructures. *Nanoscale* **6**, 5394–5401 (2014).

## ACKNOWLEDGEMENTS

The authors would like to thank Prof. Roman Gorbachev from the University of Manchester and Prof. Jose' Manuel Caridad from University of Salamanca for their useful input in improving the manuscript. This work is supported by the Austrian Science Fund (FWF) under grants no. I4323-N36 and Y1298-N, and by the Russian Foundation for Basic Research under the project no. 19-52-14006. K.W. and T.T. acknowledge support from the JSPS KAKENHI (Grant Numbers 19H05790, 20H00354 and 21H05233). A.S. and M.K. acknowledge support from the European Regional Development Fund for the "Center of Excellence for Advanced Materials and Sensing Devices" (No. KK.01.1.1.01.0001). Also, the bilateral Croatian-Austrian project funded by Croatian Ministry of Science and Education and the Centre for International Cooperation and Mobility (ICM) of the Austrian Agency for International Cooperation in Education and Research (OeAD-GmbH) under project HR 02/2020 is acknowledged. Further, the bilateral French-Austrian project funded by the Ministère de la Recherche et des Nouvelles Technologies (Amadeus PHC under project no. 42333PL, France) and the Centre for International Cooperation and Mobility (ICM) of the Austrian Agency for International Cooperation in Education and Research (OeAD-GmbH) under project FR 12/2019 is acknowledged.

## AUTHOR CONTRIBUTIONS

M.A.A., supervised by A.M., prepared the samples, carried out experiments and data analysis, with exception of NP decoration and related experiments which were carried out by T.H.T. under supervision of E.S. M.A.A. and A.M. prepared the figures. M.A.A., A.M., and R.D.R. wrote the manuscript. T.H.T., E.S., and R.D.R. interpreted the results related to NP decoration. V.M. and E.S. provided interpretations and support for the Raman spectroscopy experiments. K.W. and T.T. provided hBN crystals. O.S. provided DHTA7 molecular source. A.S. and M.A.A. prepared CVD MoS<sub>2</sub> samples under supervision of M.K. C.T., with M.A.A. and A.M. interpreted AFM related data. C.T. assisted in the final MS preparation. A.M. proposed the concept of NRN fabrication and with R.D.R. acquired the main source of funding for the study. All the authors discussed the results and reviewed the manuscript.

## COMPETING INTERESTS

The authors declare no competing interests.



## ADDITIONAL INFORMATION

**Supplementary information** The online version contains supplementary material available at <https://doi.org/10.1038/s41699-022-00356-y>.

**Correspondence** and requests for materials should be addressed to Muhammad Awais Aslam or Aleksandar Matković.

**Reprints and permission information** is available at <http://www.nature.com/reprints>

**Publisher's note** Springer Nature remains neutral with regard to jurisdictional claims in published maps and institutional affiliations.



**Open Access** This article is licensed under a Creative Commons Attribution 4.0 International License, which permits use, sharing, adaptation, distribution and reproduction in any medium or format, as long as you give appropriate credit to the original author(s) and the source, provide a link to the Creative Commons license, and indicate if changes were made. The images or other third party material in this article are included in the article's Creative Commons license, unless indicated otherwise in a credit line to the material. If material is not included in the article's Creative Commons license and your intended use is not permitted by statutory regulation or exceeds the permitted use, you will need to obtain permission directly from the copyright holder. To view a copy of this license, visit <http://creativecommons.org/licenses/by/4.0/>.

© The Author(s) 2022